Nanoscale

PAPER

View Article Online
View Journal | View Issue

Cite this: *Nanoscale*, 2014, **6**, 10243

An experimental and computational study to understand the lithium storage mechanism in molybdenum disulfide†

Uttam Kumar Sen,[a] Priya Johari,*[b] Sohini Basu,[c] Chandrani Nayak[c] and Sagar Mitra*[a]

Received 7th May 2014
Accepted 30th June 2014

DOI: 10.1039/c4nr02480j

www.rsc.org/nanoscale

The lithium storage mechanism in molybdenum disulfide (MoS_2) has been comprehensively investigated as the existing conversion-based storage mechanism is unable to explain the reason behind its high practical capacity, high polarization losses, and the change in the discharge profile after the 1st charge–discharge cycle. To resolve these issues and to gain a deeper understanding of MoS_2-based Li-ion batteries, for the first time, we have studied the reaction mechanism of the MoS_2 anode using various experimental techniques such as XRD, Raman spectroscopy, electrochemical impedance spectroscopy, XANES, and EXAFS, as well as *ab initio* density functional theory based calculations. On the basis of the results presented here, and in line with some experimental findings, we find that the reaction of MoS_2 with Li is not as simple as with usual metal oxide based conversion reactions, but that the pathway of the conversion reaction changes after the first discharge process. In the first discharge process, lithiation is initiated by a limited intercalation process, followed by a conversion reaction that produces molybdenum nanoparticles (Mo) and lithium sulfide (Li_2S). Whereas, unlike oxide-based conversion materials, MoS_2 does not transverse back during the delithiation process. Indeed, instead of MoS_2 formation, we identified the presence of polysulfur after the complete cycle. In consecutive cycles, polysulfur reacts with lithium and forms Li_2S/Li_2S_2, and this Li–S reaction is found to be highly reversible in nature and the only source of the high practical capacity observed in this electrode. To validate our experimental findings, an atomic scale *ab initio* computational study was also carried out, which likewise suggests that Li first intercalates between the MoS_2 layers but that after a certain concentration, it reacts with MoS_2 to form Li_2S. The calculations also support the non-reversibility of the conversion reaction, by showing that Mo + Li_2S formation is energetically more favorable than the re-formation of MoS_2 + Li.

Introduction

Conversion-reaction-based materials are considered to be a potential alternative to the intercalation-based carbon anode in lithium-ion batteries.[1,2] Most of the transition metal oxides/sulfides undergo conversion reactions with Li and produce metal nanoparticles and lithium oxide/sulfide.[3] In recent years, transition metal sulfides (*e.g.*, CoS, MoS_2, WS_2)[4–8] have garnered more interest than their analogous oxides as lithium-ion battery anodes, since sulfide anodes exhibit less polarisation losses compared to oxides. It has been observed that the M–X (metal–anion) bond polarity is one of the main reasons behind the polarisation loss, and as metal–sulfide bonds are less polar than metal–oxide bonds, the polarisation loss decreases from the oxide to sulfide materials.[9,10] Among these sulfides, MoS_2 is the most studied system, as it can exhibit high reversible capacity with excellent cyclic stability. Extensive work has been done to achieve an enhanced reversible capacity, better cyclic life, and high columbic efficiency of the MoS_2 electrode by putting it through a nano-structure formation,[11–14] composite formation,[15–18] and improved electrode fabrication.[11,18] MoS_2-based electrode demonstrates a stable capacity in the range of 850–900 mA h g^{-1},[11,13,14] while composite electrodes using graphene or CNTs exhibits even higher reversible capacity of around 1300 mA h g^{-1} with an improved cyclic stability.[15,16,19]

However, there are some fundamental questions which are yet to be answered such as: (a) origin of the high practical capacity over the theoretical capacity, (b) a change in the nature of the discharge profile after the 1st cycle and (c) the actual mechanism of Li storage. The calculated capacity of the

[a]*Electrochemical Energy Laboratory, Department of Energy Science and Engineering, IIT Bombay, Powai, Mumbai-400076, India. E-mail: sagar.mitra@iitb.ac.in; Fax: +91 22 2576 4890; Tel: +91 22 2576 7849*

[b]*Department of Physics, School of Natural Sciences, Shiv Nadar University, Gautam Budh Nagar, Greater Noida, Uttar Pradesh-201314, India. E-mail: priya.johari@snu.edu.in*

[c]*Atomic and Molecular Physics Division, Bhabha Atomic Research Centre, Mumbai-400085, India*

† Electronic supplementary information (ESI) available. See DOI: 10.1039/c4nr02480j

balanced reaction between MoS_2 and Li ($MoS_2 + 4Li = Mo + 2Li_2S$) is 670 mA h g^{-1}, as per the conversion reaction, whereas, the observed capacity reported in the literature is in the range of 850–1300 mA h g^{-1},[11–19] which is much higher than that of the theoretical capacity. In general, conversion based reactions themselves are complicated and need special investigation to understand the reaction mechanisms.[20–24] Similarly, the reaction chemistry between MoS_2 and Li is also not well explained in the literature.[11–19] Earlier reports illustrated that the MoS_2 reacts with 4 moles of Li and produces Mo nanoparticles and Li_2S ($MoS_2 + 4Li \leftrightarrow Mo + 2Li_2S$), and also claim that the reaction is reversible in nature.[15–17,25,26] Recently, a few serious efforts have been made to understand the charge discharge mechanism of the MoS_2 anode, which question the earlier mechanism and discuss a possible shift in the reaction pathway from the first cycle to the remaining cycles.[4,27–30] The use of XRD,[27,28] FTIR,[28] and TEM[27] analyses have identified the presence of elemental sulfur after the first cycle and, furthermore, the similarity in the charge discharge profile of the MoS_2 electrode (after the 1st cycle) and the Li–S battery[4,27,31,32] leads to the conclusion that after the first cycle, the reaction is mainly between sulfur and Li rather than MoS_2 and Li. However, a detailed study to understand the mechanism of Li storage in the MoS_2 electrode has not hitherto been reported and the reason behind the possible change in the reaction pathways therefore needs to be studied further.

In this report, we intend to discuss the reaction mechanism of MoS_2 and Li during the charge–discharge reaction, with the help of different experimental techniques, as well as theoretical studies. MoS_2 prepared by the solid-state synthesis method was used to prepare the electrode, which was tested against Li. Different *in situ* and *ex situ* techniques were employed to investigate the lithiation–delithiation process. The end products of the charge–discharge cycles were analysed by using *ex situ* XRD and Raman spectroscopy. The electronic state of Mo was determined by XAFS analysis, while the electrochemical impedance spectroscopy (EIS) was carried out during the progress of the reaction, to predict the electrochemical environment within the electrode. The reaction mechanism for the MoS_2–Li reaction was proposed with the help of different characterisation techniques, and the predicted mechanism was used to explain the change in the charge–discharge profile. Furthermore, the observed behaviors were validated by simulating the lithiation–delithiation processes using an *ab initio* density function theory (DFT) based approach. The results obtained from the theoretical calculations were found to be in good agreement with the experimental results.

Experimental section

Synthesis

MoS_2 was prepared by a modified gas phase synthesis using molybdenum trioxide (MoO_3) nanobelts and sulfur. In the first step, α-MoO_3 nanobelts were prepared by a hydrothermal method using an acidic aqueous solution of sodium molybdate at 180 °C for 24 h in a 50 ml Teflon lined autoclave.[33] As-prepared MoO_3 (0.7 g) and an excess of sulfur (3 g) were loaded into two individual quartz boats, and both the boats were placed inside a two zone heating tubular furnace. MoO_3 was placed in the higher heating zone (700 °C) and sulfur was placed in the upstream side (~400 °C) of the horizontal tubular furnace. A $H_2 + N_2$ mixture (5% H_2 + 95% N_2) gas was used as the carrier gas, as well as a reducing agent. The reaction was completed in 4 h; the sample was then calcined at 850 °C for 2 h and finally allowed to cool down to room temperature under ambient conditions.

Material characterizations

Powder X-ray diffraction (XRD) measurements were carried out at room temperature (30 °C) using a Philips X′-pert diffractometer with Cu Kα radiation ($\lambda = 1.5418$ Å) at 40 kV and 40 mA. XRD analysis was used to characterize the as-prepared powder sample, as well as the thin film electrode. To identify the different phases of the electrode components, the *ex situ* XRD technique was used after the complete discharge–charge cycle.

Information from different metal–sulfur vibrational modes were obtained using a Raman spectrometer (Jobin Yvon HR800) with a 514.5 nm laser at 10 mW power. Similar to the XRD analysis, Raman spectroscopy was also done for the as-prepared powder sample and thin film electrode after different charge–discharge cycles.

A field emission gun scanning electron microscope (FEG-SEM, JEOL-7600F) with a resolution of about 1 nm was used to study the surface morphology of the samples. Further investigations were done using a high resolution field emission transmission electron microscope (HR-TEM, JEOL-2100F). For the SEM analysis, a powder sample was sprinkled over a carbon film and images were taken at the best operating conditions. For TEM analysis, a well-dispersed solution was prepared by adding a pinch of MoS_2 powder in acetone and the solution was ultrasonically dispersed for 10–15 min. One drop of the well-dispersed solution was taken to the TEM grid, in order to take the images at the best operating conditions.

X-ray absorption fine structure (XAFS) measurements were carried out on the MoS_2 electrode before cycling (*i.e.*, pristine MoS_2), after a half cycle (*i.e.*, after the first discharge process), and after ten cycles (*i.e.*, after ten charge–discharge cycles), and at the Mo–K (20 000 eV) edge at the energy scanning EXAFS beamline (BL-9), INDUS-2 Synchrotron Source (2.5 GeV, 120 mA), Raja Ramanna Centre for Advanced Technology (RRCAT), Indore, India.[34] The samples were in the form of a thin film of thickness around 50 microns on a Cu foil of thickness of 9 micron.

The Scanning EXAFS beamline (BL-9) covers a photon energy range of 4–25 KeV and has a resolution ($E/\Delta E$) of 10 000 at 10 KeV. The beamline uses a double crystal monochromator (DCM) with a Rh/Pt coated cylindrical pre-mirror for vertical collimation of the beam. The second crystal of the DCM, which is a sagittal cylinder with a radius of curvature in the range of 1.28–12.91 meters, provides horizontal focusing to the beam. For measurements in the fluorescence mode, the sample was placed at 45° to the incident beam. An ionization chamber placed before the sample measures the incident flux (I_0), and a

vortex Si drift detector placed at 90° to the incident beam measures the intensity of the fluorescence emitted by the sample (I_f). From these intensities, the absorbance of the sample can be found as a function of energy.

Electrochemical cell fabrication and measurements

Galvanostatic charge–discharge testing was carried out in a Swagelok type cell assembly with a half-cell configuration like Li/electrolyte/MoS_2. The cells were assembled in an argon-filled glove box (Lab Star, Mbraun, Germany) with moisture and oxygen levels of ~1 ppm. A thin Li foil was used as the counter, as well as the reference electrode. The electrolyte used in this case was 1 M $LiPF_6$ in EC/DMC (1 : 1 weight ratio) (LP-30, Merck, Germany). Borosilicate glass microfiber filters (GF/D, Whatman) with a thickness of 0.67 mm and a pore size of 2.7 μm was used as the separator. The electrodes were prepared by using MoS_2 as the active material, carbon black (Super C-65, Timcal, Switzerland) as a conductive additive, and a polymeric binder (sodium salt of carboxymethyl cellulose, CMC), in an overall ratio of 60 : 20 : 20. Cu foil of 9 micrometer (μm) thickness was used as the current collector. The cyclic voltammetry (CV) profile was obtained by measuring the *i–V* response at a scan rate of 0.2 mV s^{-1} within the potential limit of 0.01 V–3.0 V *vs.* Li/Li^+, using a Bio-logic VMP-3 model. The electrochemical charge–discharge test was performed using an Arbin Instrument, USA (BT2000 model), at a current density of 200 mA g^{-1}, within a voltage cut off of 3.0 V and 0.01 V *vs.* Li/Li^+. All the electrochemical measurements were done at a constant temperature of 20 °C. Electrochemical impedance spectroscopy (EIS) was carried out at different potentials during the charge–discharge process using a Bio-logic VMP-3 instrument. During the entire process, the cell was never disconnected from the circuit, and we termed this technique as *in situ* impedance spectroscopy (*i.e.*, continuous impedance spectroscopy). Five different potential points were selected for the EIS measurements, namely 1.0 V, 0.5 V and 0.2 V *vs.* Li/Li^+ during the discharge process, and 2.0 V and 2.7 V *vs.* Li/Li^+ during the charge process. In the first cycle, EIS were taken at six points, which include open circuit voltage (OCV) along with five different potentials as discussed above. At each point, the potentiostatic EIS was taken within a frequency range of 1 MHz to 0.1 Hz and with $\Delta V = 5$ mV. For the EIS measurements, the charge–discharge was carried out at a current density of 50 mA g^{-1}.

For *ex situ* characterization, charge–discharge cycles were done in Swagelok type cells, as these are easy to open. Electrodes were charged and discharged at a slower rate of 50 mA g^{-1}. After complete charge–discharge cycles, the cells were opened inside the argon filled glove box and the thin film electrode was washed with diethyl carbonate (DEC) to remove the electrolyte, and finally dried at 60 °C in vacuum for 12 h inside the glove box.

Computational details

To confirm the experimental findings and to understand the evolution of the system with the lithiation and delithiation of the MoS_2 anode in detail, we performed *ab initio* density functional theory (DFT) based calculations using the Vienna Ab-Initio Simulation Package (VASP).[35,36] In our calculations, projector-augmented-wave (PAW)[37] potentials were used to account for the electron-ion interactions, while electron exchange–correlation (xc) interactions were treated using a generalized gradient approximation (GGA) in the Perdew–Burke–Ernzerhof (PBE) version.[38] The lithiation–delithiation process was modeled by manually inserting/removing the Li atoms at/from different locations between the layers of the bulk MoS_2/(Mo + Li_2S) and then letting the structure be optimized. Since we considered a bulk system, no vacuum was inserted along the *x*, *y*, and *z*-directions and the system was kept periodic along all three directions.

To study the lithiation process, 1 to 8 Li atoms per MoS_2 layer were inserted at different locations in between the layers of MoS_2, arranged in AB staking. The unit cell contains two MoS_2 units separated by at least 4.21 Å (ref. 39) (the optimized distance between the MoS_2 layers in bulk MoS_2), with Li intercalated between them. The unit cell, as well as the atoms, were both allowed to relax. The unit cell relaxation was performed by varying the dimensions and shape of the cell, while atoms were allowed to relax until the atomic forces were less than 0.01 eV $Å^{-1}$. In most of the plane wave codes, volume and cell optimization generally affects the calculations of Pulay stress,[35,36] leading to incorrect calculations of the diagonal components of the stress tensor. A high energy cut-off for the plane wave basis sets is therefore needed in such calculations to obtain a reliable stress tensor. Hence, we used an energy cut-off of 520 eV throughout our calculations.

During the calculations, we found that with the increase in Li concentration, the unit cell mainly expands in the *z*-direction, but relatively less or in equal amounts along the *x*- and *y*-directions. The *k*-point mesh was therefore chosen according to the dimension of the cell. Since the lattice vectors along the *x*- and *y*-directions remain the same, we chose 15 *k*-points along both of these directions, while in the *z*-direction, the *k*-points mesh was changed as per the variation in the dimension of the unit cell along the *z*-axis. In general, for low concentrations of Li atoms (1 or 2 Li/MoS_2 layer), a *k*-points mesh of 15 × 15 × 15 was considered, while, depending on the size of the system in the *z*-direction (note: the *z* lattice vector is longer than the *x* and *y*), *k*-mesh of 15 × 15 × 5 or 15 × 15 × 3 or 15 × 15 × 1 were used for systems having higher Li concentration (3–8 Li atoms/MoS_2 layer).

Similarly, to examine the delithiation process, Li atoms were gradually removed from a few of the optimized MoS_2–Li configurations such as MoS_2–2Li, MoS_2–4Li, and MoS_2–14Li, which contain 1, 2, and 7 Li atoms per MoS_2 layer, respectively. The atoms were removed from various locations and then both atoms, as well as the unit cell, were again allowed to relax and attain the optimized geometry. With the removal of Li atoms, the *k*-points mesh also changed accordingly.

Experimental results

A pure phase of MoS_2 powder was prepared by modified gas phase synthesis. The XRD pattern shown in Fig. 1(a) is indexed as the hexagonal phase of MoS_2 (JCPDS card no. 77-1716).

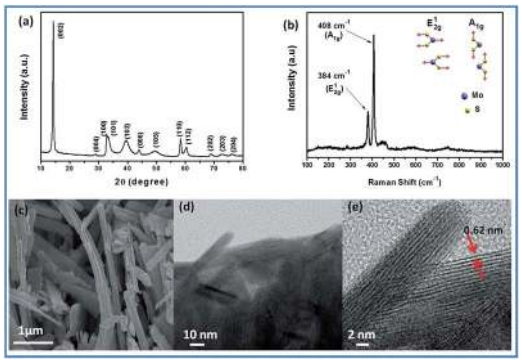

Fig. 1 (a) X-ray diffraction study, (b) Raman spectroscopy study of as-prepared MoS_2, (c) FEG-SEM, and (d and e) FEG-TEM images of MoS_2 nanobelts prepared in 5% H_2 atmosphere.

Raman analysis (shown in Fig. 1(b)) also confirms the formation of pure MoS_2. MoS_2 exhibits two sharp peaks at 384 cm^{-1} (E^1_{2g}) and 408 cm^{-1} (A_{1g}), respectively, which are due to the first-order Raman vibrational modes within the S–Mo–S layer. Both the XRD and Raman analyses show that there was no oxide impurity in the sample.

A high resolution scanning electron micrograph was used to determine the morphology of MoS_2. Belt-like MoS_2 particles were observed with a width of ~200 nm, whereas the length was in the micrometer range (Fig. 1(c)). To have a better idea of these nanobelts, FEG-TEM imaging was done. Careful observation shows that very small nanorods with a diameter of ~10 nm were embedded inside the belts (Fig. 1(d) and (e)).

Electrochemical results

The MoS_2 electrode was tested against metallic Li in a half-cell configuration. The cyclic voltammogram of the half-cell is shown in Fig. 2(a). During the first cathodic sweep, two prominent peaks were observed at 1.1 V and 0.3 V *vs.* Li/Li^+, while during the anodic sweep, one prominent peak at 2.3 V, and two small peaks at 1.45 V and 1.7 V were observed. In the consecutive cycles, the anodic peaks remain unchanged, whereas prominent changes were observed during the cathodic sweep. An extra cathodic peak at 1.8 V was observed in the 2nd cycle, which was split into two peaks after a few cycles. It was also observed that the cathodic peak positions at 1.1 V and 0.3 V were shifted from the 1st cycle to the 2nd cycle to the remaining cycles. The explanations given in the literature for the origin of these peaks are debatable. According to most of the literature reports,[15–17,25,26] the cathodic peak in the range of 1.1 V to 0.9 V was due to the intercalation of Li ions, whereas the peak in the range of 0.3–0.5 V was due to the conversion reaction between MoS_2 and Li. Similarly, the anodic peak at ~2.3 V was known for MoS_2 formation from Li_2S and Mo, and the small peaks in the range of 1.4 V to 1.8 V were assigned to the multistep deintercalation reaction.[15,17,25,26,40] The origin of the cathodic peak in the range of 1.8 V to 1.95 V during the second cycle was assigned to the formation of a gel-like polymeric layer.[15,40,41] Recent reports have raised question on these explanations, as the authors have found that the obtained results are similar to the lithium–sulfur battery.[14,30] It is evident from the available literature that the first discharge reaction occurs in two steps: intercalation of Li^+ into the interlayer spacing of MoS_2, followed by the conversion reaction that produces Mo nano-particles and Li_2S. However the delithiation reaction is not properly understood, since there is a possibility of the formation of either MoS_2 or polysulfur. Also, the possibility of having a different delithiation mechanism altogether cannot be ruled out. Outlines of the various possibilities for the MoS_2–Li reaction are presented in Scheme 1.

The above discussion shows that the actual reaction pathway for the MoS_2–Li reaction is not yet clear. Therefore, to understand the underlying reaction mechanism, we performed XRD, Raman spectroscopy, and XAFS analyses on the end product of the reaction after discharge–charge cycling, and the results are discussed in the following sections.

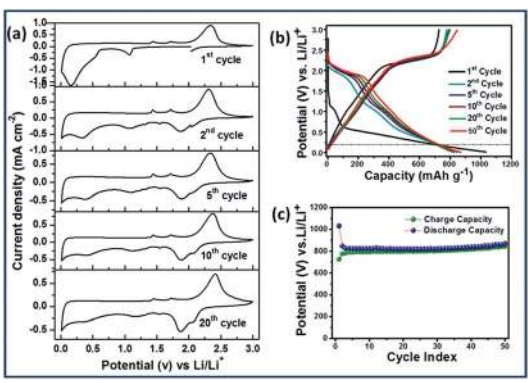

Fig. 2 (a) Cyclic voltammogram, (b) charge–discharge profile at 200 mA g^{-1} current rate, and (c) cyclic performance of MoS_2 anode in the range of 3.0 V to 0.01 V *vs.* Li/Li^+ at a 200 mA g^{-1} current rate at 20 °C.

Ex situ XRD and Raman analysis

Ex situ XRD analysis was performed on the MoS_2 electrode before cycling and after the 1st, 2nd, and 10th discharge–charge cycles to identify the phase of the electrode material (shown in Fig. 3(a)). After the first discharge–charge cycle, it was found that the peaks corresponding to MoS_2 were absent, while new peaks at 24.93° and 33.12°, along with two small humps at 21.22° and 36.63° emerged. Upon cycling, these new XRD peaks become more

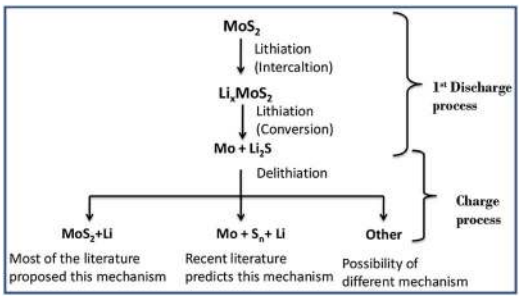

Scheme 1 Different possibilities for the charge–discharge reactions of MoS_2 with Li.

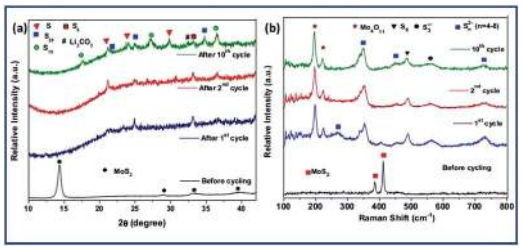

Fig. 3 (a) *Ex situ* XRD and (b) Raman spectra for MoS_2 electrode after different cycles.

intense. On careful investigation, it was found that the new peak positions were associated with various polymorphs of sulfur. However, the most significant fact is that there is no signature of MoS_2 after the first cycle. It is evident from the *ex situ* XRD analysis that after the first discharge–charge cycle, the presence of MoS_2 was not observed, but the presence of sulfur was noticed. Hence the *ex situ* analysis suggests that the delithiation reaction does not lead to the formation of MoS_2 as a reconversion product, and, therefore, the possibility of the Mo + Li_2S → MoS_2 + Li reaction route is questionable.

To validate the XRD results, Raman analyses were performed on the same samples in *ex situ* mode. As the electrode material may become amorphous (or nano-crystalline) after the conversion reaction, and as a result, XRD analysis might fail to characterize all the phases present in the electrode sample. On the other hand, Raman spectroscopy is independent to material crystallinity and can provide better information of amorphous materials as it observes vibrational, rotational and other low-frequency modes in a system. Hence Raman spectroscopy was considered as a more relevant technique for this study. Raman analysis (Fig. 3(b)) also shows that after the first cycle (discharge–charge) there was no signature of MoS_2, while peaks associated with elemental sulfur and polysulfide were observed. After the first discharge–charge cycle, the peaks at 384 cm^{-1} and 408 cm^{-1} disappeared, and these are the characteristic peaks of MoS_2. At the same time, new peaks emerged at 195 cm^{-1}, 219 cm^{-1}, 268 cm^{-1}, 347 cm^{-1}, 449 cm^{-1}, 484 cm^{-1}, 565 cm^{-1}, and 729 cm^{-1}, respectively. The new peaks at 195 cm^{-1} and 219 cm^{-1} were assigned to $Mo_{11}O_4$.[42] Since the Raman experiments were performed in the *ex situ* mode, hence during sample loading, the possibility of air oxidation of the metal nanoparticles cannot be excluded. The Raman shift observed at 268 cm^{-1}, 347 cm^{-1}, 449 cm^{-1}, and 729 cm^{-1} are an indication of the presence of polysulfide anions.[43–45] The presence of elemental sulfur was supported by the Raman shift at 484 cm^{-1}.[43–45] In addition, the *ex situ* Raman analysis does not support the reaction mechanism of MoS_2 formation, as expected. The presence of polysulfide anions along with polysulfur strongly suggest the reaction mechanism of Mo + Li_2S → Mo + S_n + Li, along with some auxiliary reaction that supports the formation of polysulfide anions.

Ex situ XANES and EXAFS analyses

From the above XRD and Raman analyses, the existence of elemental sulfur as a reaction product (after the first discharge–charge cycle) is confirmed. It was also observed that the presence of MoS_2 was absent after the first cycle of the discharge–charge process. Therefore, it can be concluded that after the 1st discharge–charge cycle, the end reaction product contains sulfur, not MoS_2. Now the question arises, what is the state of Mo in the reaction product? To determine the state of Mo before and after cycling (after 10 cycles), the Mo K-edge was probed by a highly sensitive technique, such as the X-ray absorption near edge structure (XANES) technique.

The X-ray absorption edge of a metal atom changes from its elemental state when it takes part in the formation of a compound. Generally, the absorption edge is shifted to higher energy as the core electron binding energy increases with the metal atom transforming to a positive ion while participating in the formation of a chemical bond. This energy shift (ΔE) increases with an increase in the oxidation state or positive charge on the metal ions. Thus, as the valence or oxidation state of the metal increases, the absorption edge ideally should shift towards a higher value.[46]

Fig. 4 shows the Mo K-edge spectra of the MoS_2 electrode before cycling, after the first discharge, and after 10 discharge–charge cycles. The as-prepared MoS_2 sample is treated as a reference which contains Mo in 100% +4 oxidation state. The absorption edge of the sample after the 10th cycle (discharge–charge) was shifted towards a higher value (determined by the maxima of the first derivative of the edge) and has a pre-edge feature which is a characteristic of the MoO_3 structure. The existence of the pre-edge peak is related to the local symmetry around the Mo atoms. The distortion from an ideal octahedral symmetry removes the inversion center and induces hybridization between the p and d orbitals. As a consequence, a distinct pre-edge peak occurs due to the transition from the core 1s level to the unoccupied 4d state.[47] Therefore, the oxidation state of Mo in this sample was close to +6. To get a better insight into the sample, an extended X-ray absorption fine structure (EXAFS) spectra of MoS_2 electrode before cycling were carried out, after the first discharge process and after 10 discharge–charge cycles, as shown in Fig. 5(a). Fig. 5(a) shows the experimental μ(E) *versus* the *E* spectra for the three samples. In order to take care of the oscillations in the absorption spectra, the

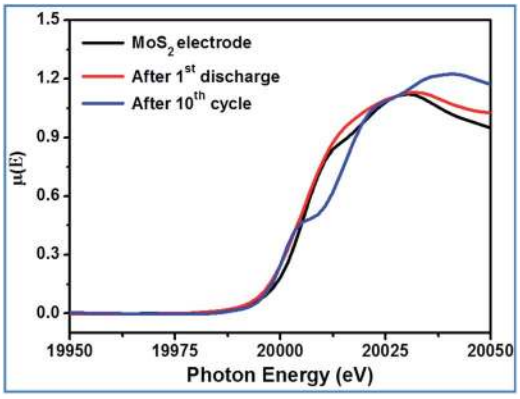

Fig. 4 Mo K-edge XANES spectra for MoS_2 electrode after different discharge–charge cycles.

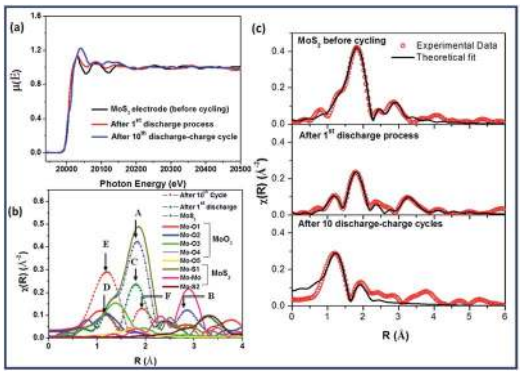

Fig. 5 (a) Normalized EXAFS spectra of MoS_2 electrode samples after different discharge cycles, (b) the experimental $\chi(R)$ *versus* R spectra and the theoretical paths generated from both MoO_3 and MoS_2 standard structures, and (c) experimental $\chi(R)$ *versus* R spectra and the theoretical fits of MoS_2 electrode before cycling, after the 1st discharge process, and after 10 discharge–charge cycles.

energy dependent absorption coefficient $\mu(E)$ was converted to the absorption function $\chi(E)$, defined as follows:

$$\chi(E) = \frac{\mu(E) - \mu_0(E)}{\Delta\mu_0(E_0)}$$

where, E_0 is the absorption edge energy, $\mu_0(E_0)$ is the bare atom background, and $\Delta\mu_0(E_0)$ is the step in the $\mu(E)$ value at the absorption edge. After converting the energy scale to the photoelectron wave number scale (k) as defined by:

$$k = \sqrt{\frac{2m(E - E_0)}{\hbar^2}}$$

the energy dependent absorption coefficient $\chi(E)$ was converted to the wave number dependent absorption coefficient $\chi(k)$, where m is the electron mass. Finally, $\chi(k)$ is weighted by k to amplify the oscillation at high k, and the $k\chi(k)$ functions are Fourier transformed in R space to generate the $\chi(R)$ *versus* R (or FT-EXAFS) spectra in terms of the real distances from the center of the absorbing atom. It should be mentioned here, that a set of EXAFS data analysis programs available within the IFEFFIT software package were used for the reduction and fitting of the experimental EXAFS data.[48] This includes data reduction and Fourier transform to derive the $\chi(R)$ *versus* R spectra from the absorption spectra (using ATHENA software), generation of the theoretical EXAFS spectra starting from an assumed crystallographic structure, and finally fitting of the experimental data with the theoretical spectra using the FEFF 6.0 code (using ARTEMIS software). The structural parameters for MoS_2 and MoO_3 used for simulation of the theoretical EXAFS spectra were taken from the reported values in the literature.[49,50] The fittings were carried out using the IFEFFIT code (which uses a non-linear least-squares method to fit the experimental data) with R (bond distance), CN (neighboring shell co-cordination number), and σ^2 (Debye–Waller factor) as fitting parameters and the typical uncertainties involved are of the order of 0.05 Å for R, 0.1 for CN, and 0.001 for σ^2.

In order to determine the appropriate standard structure from the two possibilities (MoO_3 and MoS_2), we started the initial fitting of the experimental data for each sample; the first few scattering paths were generated theoretically and plotted along with the FT-EXAFS data in R space as shown in Fig. 5(b). It should be mentioned here that the peak positions in the R space differ from the actual bond length values by a phase factor, which generally amounts to an increase of ~0.3–0.5 Å from the peak position values, depending on the type of the nearest neighbor scatterer. It is evident that the peaks corresponding to the as-prepared MoS_2 sample, especially the first major peak at ~1.9 Å, indeed coincides with the theoretical nearest Mo–S single scattering (SS) path, and the second major peak at ~2.9 Å converges with the next nearest Mo–Mo SS path (denoted by peaks A and B in Fig. 5(b)). However, when the sample has undergone a discharge–charge cycle, the amplitude of the peak corresponding to the Mo–S SS path was reduced considerably and a new peak emerged at a lower radial distance of ~1.2 Å, which matches with the nearest Mo–O SS path arising from the MoO_3 structure (denoted by peaks C and D in Fig. 5(b)). Thus, there is a clear indication that both MoO_3 and MoS_2 states were present in this case. On the other hand, after the sample was cycled 10 times, the Mo–O peak at 1.2 Å became dominant and the Mo–S peak reduced significantly (denoted by peaks E and F in Fig. 5(c)). A smaller peak at ~2.0 Å was probably due to the farther Mo–O SS paths (Mo–O_4 and Mo–O_5 paths). Thus we can conclude that the contribution of MoS_2 decreases as the sample undergoes an increasing number of discharge–charge cycles, and Mo goes from +4 oxidation state in MoS_2 to +6 oxidation state in MoO_3 after 10 discharge–charge cycles. This has also been observed previously from high resolution XANES measurements at the Mo–K edge on similar samples, as discussed earlier.

Finally, the EXAFS fitting was carried out with the MoS_2 structure for the as-prepared MoS_2 sample, with a combination of MoS_2 and MoO_3 structures for the sample cycled once, and with the MoO_3 structure for the sample after 10 discharge–charge cycles; and here, satisfactory fits were obtained with reasonably good fitting quality factors. Fig. 5(c) shows the experimental $\chi(R)$ *versus* R spectra, and the theoretical fits of the samples. The gradual changes in the amplitude of the different peaks are also evident from Fig. 5(c). The best fit parameters are presented in Table T1 as ESI.† It should be noted that, for the sample after 10 discharge cycles, the fit was carried out up to the first two peaks in the R space. The fit quality for this sample was poorer and the fitting range was smaller than for the other two, which indicates a more disordered environment in the sample.

From the EXAFS analysis, it was found that after a few cycles of the discharge–charge process, there was no signature of Mo–S bond. Mo–O bonds are observed due to the oxidation of metal nanoparticles in the presence of atmospheric oxygen. Since metal nanoparticles are known to be highly reactive, Mo nanoparticles are oxidized in the atmospheric condition to produce molybdenum oxide. Due to the same reason, the presence of Mo–O bonds was observed in the first discharge product where only metal nanoparticles were supposed to be present. Some extent of Mo–S bonds was also found after the

first discharge process due to the presence of unreacted MoS_2 in the discharge product. From the above analysis, it is evident that Mo–S bonds are broken during the lithiation process; whereas, Mo–S bonds are not developed during the reverse reaction. Therefore it can be concluded that the re-formation of MoS_2 in this electrochemical system is unlikely.

Electrochemical impedance spectroscopy (EIS)

EIS is a well-known technique to understand the overall electrode properties and the electrochemical changes that occur within the electrode. To know the electrochemical environment within the electrode during the charge–discharge process, an *in situ* impedance spectroscopy (or continuous impedance spectroscopy) was performed at five different points. Three points were taken during the discharge process at 1.0 V, 0.5 V, and 0.2 V *vs.* Li/Li^+, whereas two points were taken during the charge process at 2.0 V and 2.7 V *vs.* Li/Li^+, respectively.

To determine what changes have occurred in the cell during the discharge–charge cycling, the EIS were taken at five different points (mentioned above) for the 1st cycle, 2nd cycle, 10th, and 11th cycle, as shown in Fig. 6. It was observed that in the first discharge cycle after 0.5 V, two semi circles were formed, which signify the possible presence of two phases in the system and that could be Li_2S and unreacted MoS_2 (or lithiated MoS_2). But the nature of the EIS spectra of the discharge process changed from the 1st cycle to the 2nd cycle, which implies that after the first cycle there was a change in the lithiation process. The EIS spectra of the lithiation process remained unchanged thereafter, indicating that after a few initial cycles, the lithiation reactions were stabilized. On the other hand, the EIS of the charge profile (delithiation process) does not show any significant changes. This was also reflected in the charge–discharge profile, as well as in the cyclic voltammogram, which suggests that during the charging process, the reactions were unchanged from the 1st cycle to the remaining cycles. Hence, it can be concluded from the EIS study that there was a significant change in the lithiation process (discharge process) from the 1st cycle to the remaining cycles, whereas for the delithiation process (charge process), the process remains the same. The EIS results are in good agreement with the above XRD and Raman analyses, which confirms the possible shift in the lithiation process from the 1st cycle to the remaining cycles.

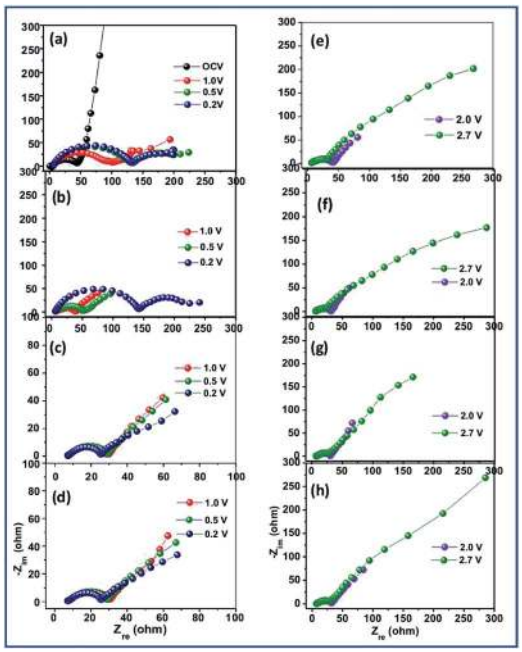

Fig. 6 EIS spectra of the MoS_2 electrode at different states of charge during the discharge process for (a) 1st cycle, (b) 2nd cycle, (c) 10th cycle, (d) 11th cycle and during the charge process for (e) 1st cycle, (f) 2nd cycle, (g) 10th cycle and (h) 11th cycle. (Details are given in the materials characterization section). Note that (c) and (d) are plotted on different scales for better clarity.

Discussion

From the above experimental results, it could be argued that the reaction mechanism proposed in earlier reports, $MoS_2 + xLi \leftrightarrow Li_xMoS_2 + Li \leftrightarrow Mo + Li_2S$ as a reversible reaction, is not true in actual fact. Indeed, it seems that the given reaction is only applicable for the first discharge cycle, where MoS_2 reacts with Li to form Mo and Li_2S, but the reverse reaction is not profound. During the reverse reaction (charge process), Li_2S breaks to Li and polysulfur, as confirmed by the XRD and Raman spectra. Mo remains in the atomic or ionic form Mo^{+6} (as Mo^{+6} is the most stable state), as shown from the XAFS analysis. In the consecutive cycle, polysulfur reacts with Li to form Li_2S, and this Li–S reaction was found to be reversible. EIS also suggested that the electrochemistry of the discharge reaction (lithiation process) changes from the 1st cycle to the remaining cycles, whereas the delithiation process remains the same for all the cycles. Based on this mechanism, the obtained CV result (Fig. 2(a)) can be explained. In the first cathodic sweep (discharge process), Li intercalation was performed at ~1.1 V *vs.* Li/Li^+, followed by the conversion reaction of MoS_2 and Li at ~0.3 V, leading to the formation of Mo and Li_2S. During the anodic sweep (charge process), the main reaction was the formation of sulfur from Li_2S, which gives rise to the prominent peak at 2.3 V. Two small peaks at 1.45 V and 1.70 V were observed in the anodic process, whereas their corresponding cathodic peaks were observed at 1.32 V and 1.55 V, respectively. The 1.32/1.45 V and 1.55/1.70 V *vs.* Li/Li^+ redox couples were due to formation and breakage of Mo^{+6} and polysulfide ionic bonds. In the consecutive discharge cycles, the anionic peaks at 1.9 V and 1.1 V were due to the reaction of Li and polysulfur. The anionic peak at 1.9 V was found to be split into two peaks at 1.9 V and 2.1 V, respectively. The peak at 2.1 V is due to formation of Li_2S_n ($n > 4$), whereas the peak at 1.9 V is due to the formation of Li_2S_2. The peak at 1.1 V is assigned to the formation of Li_2S. The peak at ~0.3 V is associated to the reaction of Li and unreacted MoS_2, and it has been observed that the intensity of the 0.3 V peak diminishes gradually due to the unavailability of MoS_2 upon cycling. Similar observations were also made from the charge–discharge profile shown in Fig. 2(b). Hence, it can be concluded that the profile of the charge–discharge reaction changed to the Li–S reaction after the 1st cycle.

Though the above experimental results were helpful to reveal the charge–discharge mechanism of the MoS_2 electrode, the reason behind such a different behavior of the sulfide materials is yet to be understood. In the current state, the experimental analysis is not sufficient to explain why sulfide materials behave differently than oxides or why the formation of MoS_2 from Mo and Li_2S is not favorable in this electrochemical environment. To find the answer to these questions and to obtain the information at the atomic level, density functional theory (DFT) based calculations were performed on this system.

Computational study

We modeled and simulated both the lithiation, as well as the delithiation, process to understand and verify the experimental results. To mimic the lithiation process, we performed calculations using one to eight Li atoms per MoS_2 layer and examined the variation in the structural and electronic properties of the system with respect to Li concentration. As mentioned earlier in the "Computational details" subsection, for a particular Li concentration, various configurations with different positions of Li atoms were examined in the search for the most stable geometry. We found that in systems with low Li concentrations, Li usually prefers the location underneath molybdenum, which is in agreement with an earlier report.[51]

To investigate the chemical and structural changes within the anode material during the lithiation (discharge) process, we first examined the variation in the optimized ground state energy, the total volume of the cell, and the volume/atom ratio of the optimized structures with respect to the number of Li atoms per MoS_2 layer. A linear/monotonic increase in the ground state energy (*i.e.*, in the negative direction), the volume, and the volume/atom ratio were observed when there were a 1 to 6 Li atoms/MoS_2 layer (see Fig. 7). Whereas, a sudden variation was noticed when more than 6 Li atoms were inserted in between the MoS_2 layers. We wonder if this sudden change in the trends is related to any significant change in the structure of the system. To analyze this, we investigated the optimized structures presented in Fig. 8 in more detail, and tabulated the lattice parameters of each investigated system, together with the minimum distance between the Li and S atoms (d_{Li-S}) in Table 1.

On examining the optimized structures presented in Fig. 8, we found that when Li atoms diffuse in the MoS_2 anode, they first intercalate in between the MoS_2 layers and push the layers apart with the increase in Li concentration. With roughly 4 Li atoms/MoS_2 layer, the layers were sufficiently apart that they act like a monolayer, interacting with Li atoms. When the Li concentration reached beyond 6 atoms/MoS_2 layer, we observed a significant structural change. None of the Li atoms were now intercalated between the MoS_2 layers. As can be seen from Fig. 8, at higher Li concentrations (>6 Li atoms/MoS_2), Li atoms come closer to Mo by removing S from it, and, thus, the MoS_2 layers become dissociated into a Mo thin-film (surrounded by Li atoms), and sulfur atoms. The sulfur atoms interact with surrounding Li atoms to form Li_2S (known as conversion reaction), which is in agreement with the experimental results. The reason behind this rearrangement in the structure is the shifting of Li atoms (near to MoS_2 layer) closer to the layer, which means closer to the sulfur atoms (see d_{Li-S} in Table 1). Thereby, with the increase in Li concentration, the distance between Li and S is reduced and reaches the value equivalent or below the optimized distance between them (~2.49 Å) in the bulk Li_2S phase, which leads to the dissociation of S from MoS_2 and the formation of ionic Li_2S. A clearer picture would have been obtained if we could have taken a bigger unit cell, *i.e.*, a supercell; however, those calculations are computationally very expensive and beyond the scope of the current *ab initio* work. Nevertheless, we strongly believe that the supercell calculations will not affect our analysis in a qualitative way. Our results show that this chemical change at higher Li concentrations is the reason behind the dramatic change in the structure, which is also evident from the lattice parameters, as tabulated in Table 1. A huge variation in the lattice parameters can be seen when Li atoms/MoS_2 are more than 6. Also, one can notice that the crystal structure changes from a hexagonal ($a = b \neq c$; $\alpha = \beta = 90°$, $\gamma = 120°$) to a triclinic ($\alpha \neq \beta \neq \gamma \neq 90°$) lattice system, at high Li concentrations.

To understand the electronic change that occurs due to the chemical and structural changes in the anode at higher Li concentrations during the lithiation process, we next performed Bader charge analyses and investigated if the increase in the Li concentration affected the electronic structure, and, thus, the bonding characteristics between the atoms. In a Bader charge analysis, zero flux surfaces, that are two-dimensional surfaces on which the charge density is a minimum perpendicular to the surface, are used to divide the atoms. The charge enclosed within the Bader volume gives a good approximation of the total electronic charge of an atom. In our Bader charge calculations,

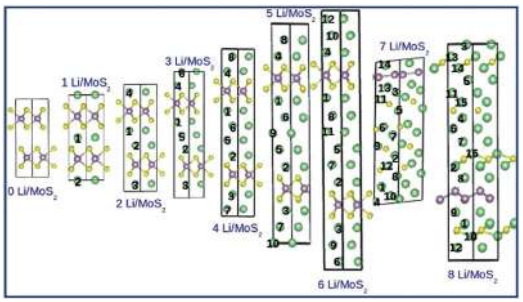

Fig. 8 Optimized structures of pristine MoS_2 and lithiated MoS_2 for various Li concentrations. The Li atoms are labeled in such a way so as to conveniently identify them in Table 2.

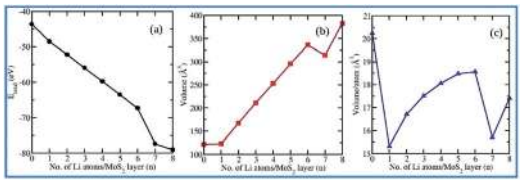

Fig. 7 Variation in (a) optimized ground state energy, (b) volume, and (c) volume per atom with respect to the number of Li atoms per MoS_2 layer.

Table 1 Lattice parameters of the optimized bulk structure of the lithiated MoS_2 anode for various Li concentrations. The shortest distance between Li and S, d_{Li-S}, is also given

No of Li atoms per MoS_2 layer	a (Å)	b (Å)	c (Å)	α	β	γ	d_{Li-S} (Å)
0	3.18	3.18	13.84	90°	90°	120°	—
1	3.23	3.23	13.57	90°	90°	120°	2.58
2	3.22	3.22	18.63	90°	90°	120°	2.54
3	3.20	3.20	23.72	90°	90°	120°	2.52
4	3.20	3.20	28.59	90°	90°	120°	2.51
5	3.19	3.19	33.54	90°	90°	120°	2.50
6	3.19	3.19	38.26	90°	90°	120°	2.49
7	4.13	4.13	21.78	80°	101°	120°	2.41–2.43
8	3.73	3.73	30.06	88°	92°	114°	2.28–2.32

both the core and the valence electrons were considered. On analyzing the net charge on each atom from Table 2, we noticed that in the case of pristine MoS_2, the charge is shared, confirming the covalent bonding between Mo and S atoms. Even with the intercalation of the single Li atom, Mo and S remain covalently bonded, with sulfur being more electronegative due to some of the charge transfer by Li atoms. With the increase in Li concentration up to six atoms, the charge on the Li atoms closer to S atoms is reduced to almost zero, showing a reduction in the ionic character of the Li atoms. Whereas, in the case of the Li atoms in the interior sites, the charge is distributed along the volume near those atoms; hence, showing electron-gas like characteristics. A sudden change in the net charge on the atoms was noticed when seven or more Li atoms/MoS_2 were inserted in between the MoS_2 layers. The negative charge on the sulfur atoms increased to ~2 from 1, while the Li atoms located near to the S atoms now carry a charge of ~+1 (see Fig. 8 and Table 2), validating the formation of Li_2S. Thus, with the increase in Li concentration, S atoms form ionic bonds with Li atoms to form Li_2S, while Mo atoms form a thin film with a negative charge that also shows metallic bonding characteristics. A few of the Li atoms that are farther from the S atoms or closer to Mo, however, remain neutral in the system, with a low charge on them or a negative charge.

To further confirm our observations about the change in bonding characteristics, we computed the electron localized function (ELF) for all the systems. ELF is defined as the localized function of the same spin-pair electron density.[53,54] The value of the ELF ranges from 0 to 1, where 1 corresponds to the localization as in covalent bonds, and 0.5 corresponds to the electron-gas-like pair probability, as in metallic bonds. Topology analysis of ELF can effectively reveal the nature of different chemical bonds. The covalent and ionic bonds are indicated by the regions of red and yellow, respectively, in the figures presented in Fig. 9. On performing topological analyses of ELF, the change in bonding characteristics of the Li atoms from metallic to ionic is also quite evident; though the clearer picture comes from the Bader charge analysis. Overall, in agreement with the experimental results, our calculations for the lithiation process confirm the formation of metallic Mo and ionic Li_2S during the first discharge process.

Simulating the delithiation process using an *ab initio* methodology is a difficult task, especially when the system has been completely distorted. In such a case, the study into the delithiation process will either be extremely expensive in terms of computational time, or there will be high chances of obtaining a metastable state or a local minima. We, however, tried to make some predictions by analyzing the trends. For this purpose, we performed calculations on selected systems with low and high Li concentrations, such as MoS_2 with one, two, and seven Li atoms/MoS_2 layer. In low Li concentrated systems, on removing Li, we re-obtained the optimized bulk MoS_2

Table 2 Net charge of Mo, S, and Li atoms for various configurations presented in Fig. 8, computed using Bader charge analyses.[52] In most of the cases, all Mo and S atoms exhibit similar charges. Therefore, instead of giving a charge to individual atoms, only the charge on one of the atom is tabulated here, while a range is given when the charge on all the atoms of a particular type of element are not the same. In the case of Li, the net charge on each Li atom is presented. The labeling of Li atoms is similar as that in Fig. 8, to enable an easy identification of the location of the Li atom in the bulk structure

n_{Li}	Mo	S	Li_1	Li_2	Li_3	Li_4	Li_5	Li_6	Li_7	Li_8	Li_9	Li_{10}	Li_{11}	Li_{12}	Li_{13}	Li_{14}	Li_{15}	Li_{16}
0	0.98	−0.49																
2	0.96	−0.90	0.85	0.85														
4	0.94	−1.00	0.53	0.53	0.53	0.53												
6	0.92	−0.99	0.15	0.15	0.15	0.15	0.78	0.78										
8	0.90	−0.98	0.06	0.06	0.06	0.06	0.48	0.48	0.48	0.48								
10	0.94	−0.99	0.10	0.10	0.10	0.10	0.35	0.35	0.35	0.35	0.17	0.17						
12	1.00	−1.02	0.07	0.07	0.07	0.07	−0.07	−0.14	0.55	0.55	0.60	0.62	−0.08	−0.14				
14	−1.23–−1.39	−1.70–−1.80	0.79	0.86	0.81	−0.98	0.85	0.85	0.86	0.82	0.84	0.76	0.82	0.83	0.80	0.79		
16	−0.78	−1.77–−1.84	0.82	0.82	0.19	0.81	−0.56	0.74	−0.48	0.81	0.81	0.82	0.76	0.07	0.81	0.81	0.81	0.81

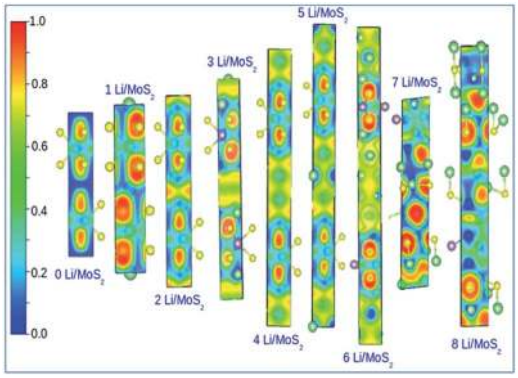

Fig. 9 Electron localized function (ELF) for all the systems depicted in Fig. 8. The red color represents covalent; yellow, ionic; and green, metallic bonding.

configuration. That means, on removing both of the Li atoms from MoS_2–2Li (one Li atom/MoS_2 layer) and relaxing the unit cell, the optimized lattice parameters of bulk MoS_2 were re-obtained. Similar results were achieved when four Li atoms were removed from MoS_2–4Li. Also, when two Li atoms were removed from MoS_2–4Li, the MoS_2–2Li structure with one Li atom intercalated between each MoS_2 layer and the same lattice parameters as of optimized MoS_2–2Li, was obtained, irrespective of the position of the Li atoms removed. Thus, our calculations predicted a reversible reaction for the intercalation process (when the Li concentration was low). However, on analyzing the delithiation process for the conversion reaction, *i.e.*, for a higher concentrated system like MoS_2–14Li (seven Li atoms/MoS_2 layer) with Mo and Li_2S, we found that, on removing Li atoms, the system with Li-intercalated in between the MoS_2 layers or the original optimized structure of that configuration cannot be retrieved. For example, on removing two Li atoms, the optimized configuration of MoS_2–12Li was not obtained (see Fig. 10(a) and (b)), and the structure remained as

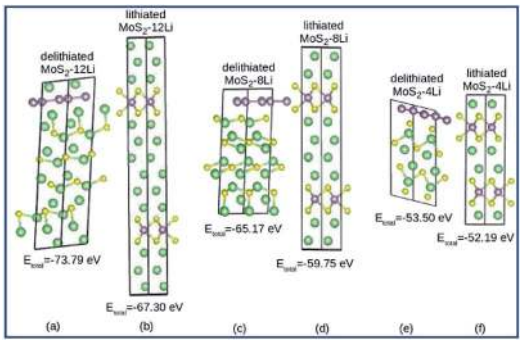

Fig. 10 Relaxed structures (a), (c), (e) obtained after removing 2, 6, and 10 Li atoms from the optimized structure of lithiated MoS_2–14Li configuration (*i.e.*, system having 7 Li atoms/MoS_2 layer), to model the delithiation process in the higher Li concentrated system. For comparison, the optimized structures (b), (d), (f) obtained from the simulation of lithiation process are also given side-by-side. The ground state energy (E_{total}) corresponding to each structure is mentioned below it.

a composition of a metallic Mo layer and ionic Li_2S, with roughly 6.5 eV larger ground state energy (~−73.79 eV) than the energy of the MoS_2–12Li system (~−67.30 eV) obtained during the first lithiation cycle, with Li atoms intercalated between the MoS_2 layers. We removed these two Li atoms from various different sites but found no reverse back to the original geometry or change in the above stated conclusion. To check if we can succeed in getting the lower Li-concentration systems back on removing more Li atoms, we extracted six and 10 Li atoms from the optimized geometry of the lithiated MoS_2–14Li system, from arbitrary locations. We, however, achieved no success and observed that Li atoms near the Mo surface prefer to diffuse out first, compared to Li atoms attached to S. The optimized geometry for delithiated MoS_2–8Li and MoS_2–4Li systems are depicted in Fig. 10(c) and (e). It is evident from the figures that on removing six or 10 Li atoms from the system that originally had 14 Li atoms, the geometry of the lithiated MoS_2–8Li and MoS_2–4Li systems (obtained during the lithiation process) cannot be retrieved. Moreover, on comparing the ground state energies (E_{total}) of the delithiated and lithiatiated systems with the same number of Li atoms/MoS_2 layers, the prior systems are found to be energetically more favorable compared to the latter ones, explaining the reason for not obtaining MoS_2 back during delithiation. Thus, our calculations also support the experimental results regarding the irreversibility of the Mo + Li_2S reaction. Once the MoS_2 layers decompose and S bonds with Li to form Li_2S, it is not possible to obtain MoS_2 back by removing Li. Though, due to the choice of smaller unit cells for obvious reasons, our calculations could not confirm the formation of different polymorphs of elemental sulfur, as found in the experiments. But we believe that calculations with a larger supercell could help to validate the above stated observations. Overall the *ab initio* computational results are in good agreement with the experimental findings and they substantially help in understanding the chemical changes that occur in the anode material during the first lithiation–delithiation (discharge–charge) cycle.

Though the above experimental results are helpful to exploit the charge–discharge mechanism of the MoS_2 electrode, the exact reason behind the high practical capacity over the theoretical capacity cannot be inferred from them. The capacity obtained from a lithium ion battery system not only arises due to the faradic reactions (or from diffusion controlled reactions, such as insertion, conversion, and alloying), but also from the non-faradic reactions (*e.g.*, capacitive reactions, such as double-layer capacitance and pseudo-capacitance),[55–60] and a few side reactions (*e.g.*, electrolyte decomposition and Li^+ adsorption on SEI layers).[61] Due to the presence of nanostructured materials and carbon particles, the capacity contribution from pseudo-capacitance is expected to be quite high. Several authors have observed that the capacity contribution from the capacitive reaction could be up to 30% to 60% to the total capacity.[60] In the current study, around 20% capacity is obtained below 0.2 V, which is mainly due to Li^+ insertion in carbonaceous species by faradic and non-faradic reactions. An even longer tail below 0.2 V can be obtained for carbon composites (*e.g.*, CNTs, graphene, and amorphous carbon)[15,16,18] of MoS_2, that exhibit

higher capacity (more than 1000 mA h g^{-1}). This clearly signifies that the larger the carbon content, higher is the capacitive contribution to the practical capacity. Hence, the actual capacity obtained from the MoS_2–Li (or Li–S) redox reaction is much lower than the theoretical capacity of 670 mA h g^{-1}.

Conclusions

In the present work we intended to study the mechanism of the lithiation–delithiation mechanism of the conversion-based MoS_2 electrode and to highlight a few significant insights into the storage mechanism. A model reaction mechanism has been proposed. On the basis of the results presented here, it may be inferred that the MoS_2–Li reaction is not reversible, unlike for other transition metal based oxides. The current mechanism suggests that in the first discharge process, MoS_2 reacts with Li *via* a conversion reaction and forms Mo nanoparticles and Li_2S, but the reverse reaction is not favourable, as isolated sulfur atoms/anions have a strong tendency to form polysulfur/polysulfides. Highly sensitive techniques like XANES and EXAFS clearly show the formation of Mo nanoparticles in the first discharge stage and no Mo–S bond formation in the complete discharge–charge stage. Furthermore, all the experiments were performed in *ex situ* mode; hence, during the sample handling and loading, Mo nanoparticles most likely are oxidized under atmospheric conditions to the highly stable form of MoO_3, as observed in the experiments. *Ab initio* density functional (DFT) calculations were carried out for the MoS_2–Li system to investigate the storage mechanism. The DFT studies reveal that Li first intercalates between the MoS_2 layers, but after a certain concentration it reacts with sulfur to form ionic Li_2S and thus separates the Mo nanoparticles. This results into a significant structural change from a hexagonal to a triclinic lattice system. These outcomes were further confirmed by using Bader charge analyses and electron localized functions. While modeling the delithiation process, we observed that the formation of MoS_2 from Mo + Li_2S is energetically less favorable. This explains the reason behind the creation of polysulfur after the delithiation process. Thus, after the first discharge cycle, the electrode no more remains as a MoS_2 anode, but rather it behaves like a sulfur electrode and the half-cell acts like a Li–S battery, which governs the reversible reaction. The proposed reaction mechanism is capable enough to explain several unanswered questions related to the MoS_2–Li system, such as the reason behind the change in the discharge profile and the high practical capacity in the MoS_2-based Li-ion battery. The current study provides an insight into another aspect of conversion based reactions and thus, yields a new opportunity to materials scientists and physicists to explore more transition metal sulfides/nitrides/phosphide electrode materials that may also exhibit a similar behavior, and hence also possess storage mechanisms that could be explained in similar fashion.

Acknowledgements

The authors (UKS and SM) are thankful to the "National Centre for Photovolatics Research and Education (NCPRE)"-*Ministry of New and Renewable Energy*, Govt. of India and IRCC-IIT Bombay for providing financial and instrumental supports. P.J. would like to acknowledge the support provided by Grant no. SR/FTP/PS-052/2012 from Department of Science and Technology (DST), Government of India. All authors are also thankful to the members of SAIF, IIT Bombay for their assistance with electron diffraction and FEG-SEM analysis, Indus Synchrotron Utilization Division, Raja Ramanna Centre for Advanced Technology, Indore, India for INDUS-2 synchrotron facility for XAFS study and Shiv Nadar University for their computational facility.

References

1 J.-M. Tarascon, S. Grugeon, S. Laruelle, D. Larcher and P. Poizot, *Lithium Batteries – Science and Technology*, ed. G. A. Nazri and G. Pistoia, Kluwer Academic, Boston, 2003, ch. 7.
2 L. Taberna, S. Mitra, P. Poizot, P. Simon and J. M. Tarascon, *Nat. Mater.*, 2006, **5**, 567–573.
3 P. Poizot, S. Laruelle, S. Grugeon, L. Dupont and J. M. Tarascon, *Nature*, 2000, **407**, 496–499.
4 T. Stephenson, Z. Li, B. Olsen and D. Mitlin, *Energy Environ. Sci.*, 2014, **7**, 209–231.
5 Y. Gu, Y. Xu and Y. Wang, *ACS Appl. Mater. Interfaces*, 2013, **5**, 801–806.
6 H. Liu, D. W. Su, G. X. Wang and S. Z. Qiao, *J. Mater. Chem.*, 2012, **22**, 17437–17440.
7 R. Bhandavat, L. David and G. Singh, *J. Phys. Chem. Lett.*, 2012, **3**, 1523–1530.
8 Y. Wang, J. J. Wu, Y. F. Tang, X. J. Lü, C. Y. Yang, M. S. Qin, F. Q. Huang, X. Li and X. Zhang, *ACS Appl. Mater. Interfaces*, 2012, **4**, 4246–4250.
9 P. G. Bruce, B. Scrosati and J.-M. Tarascon, *Angew. Chem., Int. Ed.*, 2008, **47**, 2930–2946.
10 F. Gillot, S. Boyanov, L. Dupont, M. L. Doublet, M. Morcrette, L. Monconduit and J. M. Tarascon, *Chem. Mater.*, 2005, **17**, 6327–6337.
11 U. K. Sen and S. Mitra, *ACS Appl. Mater. Interfaces*, 2013, **5**, 1240–1247.
12 S. K. Park, S. H. Yu, S. Woo, J. Ha, J. Shin, Y. E. Sung and Y. Piao, *CrystEngComm*, 2012, **14**, 8323–8325.
13 H. Hwang, H. Kim and J. Cho, *Nano Lett.*, 2011, **11**, 4826–4830.
14 M. Wang, G. D. Li, H. Y. Xu, Y. T. Qian and J. Yang, *ACS Appl. Mater. Interfaces*, 2013, **5**, 1003–1008.
15 K. Chang and W. Chen, *Chem. Commun.*, 2011, **47**, 4252–4254.
16 K. Chang and W. Chen, *ACS Nano*, 2011, **5**, 4720–4728.
17 S. Ding, D. Zhang, J. S. Chen and X. W. Lou, *Nanoscale*, 2012, **4**, 95–98.
18 X. Cao, Y. Shi, W. Shi, X. Rui, Q. Yan, J. Kong and H. Zhang, *Small*, 2013, **9**, 3433–3438.
19 K. Chang, D. Geng, X. Li, J. Yang, Y. Tang, M. Cai, R. Li and X. Sun, *Adv. Energy Mater.*, 2013, **3**, 839–844.
20 N. Pereira, L. Dupont, J. M. Tarascon, L. C. Klein and G. G. Amatucci, *J. Electrochem. Soc.*, 2003, **150**, A1273–A1280.

21 L. Wang, B. Liu, S. Ran, H. Huang, X. Wang, B. Liang, D. Chen and G. Shen, *J. Mater. Chem.*, 2012, **22**, 23541–23546.
22 L. Ji, O. Toprakci, M. Alcoutlabi, Y. Yao, Y. Li, S. Zhang, B. Guo, Z. Lin and X. Zhang, *ACS Appl. Mater. Interfaces*, 2012, **4**, 2672–2679.
23 L. Ji, Z. Lin, M. Alcoutlabi and X. Zhang, *Energy Environ. Sci.*, 2011, **4**, 2682–2699.
24 L. Ji, H. L. Xin, T. R. Kuykendall, S.-L. Wu, H. Zheng, M. Rao, E. J. Cairns, V. Battaglia and Y. Zhang, *Phys. Chem. Chem. Phys.*, 2012, **14**, 6981–6986.
25 X. Zhou, L.-J. Wan and Y.-G. Guo, *Chem. Commun.*, 2013, **49**, 1838–1840.
26 S.-K. Park, S.-H. Yu, S. Woo, B. Quan, D.-C. Lee, M. K. Kim, Y.-E. Sung and Y. Piao, *Dalton Trans.*, 2013, 2399–2405.
27 X. Fang, X. Guo, Y. Mao, C. Hua, L. Shen, Y. Hu, Z. Wang, F. Wu and L. Chen, *Chem.–Asian J.*, 2012, **7**, 1013–1017.
28 X. Fang, C. Hua, X. Guo, Y. Hu, Z. Wang, X. Gao, F. Wu, J. Wang and L. Chen, *Electrochim. Acta*, 2012, **81**, 155–160.
29 X. Fang, X. Yu, S. Liao, Y. Shi, Y.-S. Hu, Z. Wang, G. D. Stucky and L. Chen, *Microporous Mesoporous Mater.*, 2012, **151**, 418–423.
30 J. Xiao, X. Wang, X.-Q. Yang, S. Xun, G. Liu, P. K. Koech, J. Liu and J. P. Lemmon, *Adv. Funct. Mater.*, 2011, **21**, 2840–2846.
31 C. Barchasz, F. Molton, C. Duboc, J.-C. Leprêtre, S. Patoux and F. Alloin, *Anal. Chem.*, 2012, **84**, 3973–3980.
32 X. Ji and L. F. Nazar, *J. Mater. Chem.*, 2010, **20**, 9821–9826.
33 U. K. Sen and S. Mitra, *RSC Adv.*, 2012, **2**, 11123–11131.
34 D. Bhattacharyya, A. K. Poswal, S. N. Jha, Sangeeta and S. C. Sabharwal, *Nucl. Instrum. Methods Phys. Res., Sect. A*, 2009, **609**, 286–293.
35 G. Kresse and J. Furthmuller, *Comput. Mater. Sci.*, 1996, **6**, 15–50.
36 G. Kresse and J. Furthmuller, *Phys. Rev. B: Condens. Matter Mater. Phys.*, 1996, **54**, 11169–11186.
37 G. Kresse and D. Joubert, *Phys. Rev. B: Condens. Matter Mater. Phys.*, 1999, **59**, 1758–1775.
38 J. P. Perdew, K. Burke and M. Ernzerhof, *Phys. Rev. Lett.*, 1996, **77**, 3865–3868.
39 P. Johari and V. B. Shenoy, *ACS Nano*, 2011, **5**, 5903–5908.
40 S. K. Das, R. Mallavajula, N. Jayaprakash and L. A. Archer, *J. Mater. Chem.*, 2012, **22**, 12988–12992.
41 Q. Wang and J. Li, *J. Phys. Chem. C*, 2007, **111**, 1675–1682.
42 M. Dieterle and G. Mestl, *Phys. Chem. Chem. Phys.*, 2002, **4**, 822–826.
43 J. T. Yeon, J. Y. Jang, J. G. Han, J. Cho, K. T. Lee and N. S. Choi, *J. Electrochem. Soc.*, 2012, **159**, A1308–A1314.
44 M. Hagen, P. Schiffels, M. Hammer, S. Dorfler, J. Tubke, M. J. Hoffmann, H. Althues and S. Kaskel, *J. Electrochem. Soc.*, 2013, **160**, A1205–A1214.
45 B. Meyer, *Chem. Rev.*, 1976, **76**, 367–388.
46 D. Joseph, A. K. Yadav, S. N. Jha and D. Bhattacharyya, *Bull. Mater. Sci.*, 2013, **36**, 1067–1072.
47 J.-H. Kang, S.-M. Paek and J.-H. Choy, *Bull. Korean Chem. Soc.*, 2010, **31**, 3675–3678.
48 M. Newville, B. Ravel, D. Haskel, J. J. Rehr, E. A. Stern and Y. Yacoby, *Phys. B*, 1995, **208**, 154–156.
49 R. G. Dickinson and L. Pauling, *J. Am. Chem. Soc.*, 1923, **45**, 1466–1471.
50 T. Leisegang, A. A. Levin, J. Walter and D. C. Meyer, *Cryst. Res. Technol.*, 2005, **40**, 95–105.
51 H. J. Chen, J. Huang, X. L. Lei, M. S. Wu, G. Liu, C. Y. Ouyang and B. Xu, *Int. J. Electrochem. Sci.*, 2013, **8**, 2196–2203.
52 G. Henkelman, A. Arnaldsson and H. Jonsson, *Comput. Mater. Sci.*, 2006, **36**, 354–360.
53 A. D. Becke and K. E. Edgecombe, *J. Chem. Phys.*, 1990, **92**, 5397–5403.
54 B. Silvi and A. Savin, *Nature*, 1994, **371**, 683–686.
55 M. Osiak, H. Geaney, E. Armstrong and C. O'Dwyer, *J. Mater. Chem. A*, 2014, **2**, 9433–9460.
56 K. Zhu, Q. Wang, J.-H. Kim, A. A. Pesaran and A. J. Frank, *J. Phys. Chem. C*, 2012, **116**, 11895–11899.
57 T. Brezesinski, J. Wang, S. H. Tolbert and B. Dunn, *Nat. Mater.*, 2010, **9**, 146–151.
58 A. G. Dylla, G. Henkelman and K. J. Stevenson, *Acc. Chem. Res.*, 2013, **46**, 1104–1112.
59 V. Augustyn, J. Come, M. A. Lowe, J. W. Kim, P.-L. Taberna, S. H. Tolbert, H. D. Abruna, P. Simon and B. Dunn, *Nat. Mater.*, 2013, **12**, 518–522.
60 C. Hou, X.-Y. Lang, G.-F. Han, Y.-Q. Li, L. Zhao, Z. Wen, Y.-F. Zhu, M. Zhao, J.-C. Li, J.-S. Lian and Q. Jiang, *Sci. Rep.*, 2013, **3**, 2878.
61 P. Arora, R. E. White and M. Doyle, *J. Electrochem. Soc.*, 1998, **145**, 3647–3667.

